

# Advanced Micronutrient Imaging in Plants: The POLYX Beamline at the NSRC SOLARIS JU

M. PYPKA<sup>a</sup>, A. BARABASZ<sup>a</sup>, K. SOWA<sup>b</sup>, P. WRÓBEL<sup>b,c</sup>,  
T. KOŁODZIEJ<sup>b</sup>, P. KORECKI<sup>d</sup> AND O. SIEMIANOWSKI<sup>a,\*</sup>

<sup>a</sup>University of Warsaw, Faculty of Biology, Institute of Experimental Plant Biology and Biotechnology, Department of Plant Metal Homeostasis, Miecznikowa 1, 02-096 Warsaw, Poland

<sup>b</sup>National Synchrotron Radiation Centre SOLARIS, Jagiellonian University, Czerwone Maki 98, 30-392 Kraków, Poland

<sup>c</sup>AGH University of Krakow, Faculty of Physics and Applied Computer Science, Mickiewicza 30, 30-059 Kraków, Poland

<sup>d</sup>Jagiellonian University, Institute of Physics, Łojasiewicza 11, 30-348 Kraków, Poland

Received: 29.30.2025 & Accepted: 02.12.2025

Doi: [10.12693/APhysPolA.149.S218](https://doi.org/10.12693/APhysPolA.149.S218)

\*e-mail: [o.siemianowski@uw.edu.pl](mailto:o.siemianowski@uw.edu.pl)

Micronutrients such as Zn, Cu, Fe, and Mn play essential roles in plant physiology, yet their low concentrations and tissue-specific distributions pose significant analytical challenges. While various imaging techniques exist, most either sacrifice resolution for throughput or lack the ability to quantify elemental co-localization across scales. In this study, using the POLYX beamline at the National Synchrotron Radiation Centre SOLARIS, we applied micro X-ray fluorescence ( $\mu$ XRF) mapping to investigate the spatial distribution and co-localization of Zn, Cu, Fe, Mn, and Ca in the root system. Whole-root scans at 100  $\mu$ m resolution provided an overview of elemental architecture, while selected regions imaged at 5  $\mu$ m resolution revealed tissue-level heterogeneity. To interpret elemental relationships, we generated overlap matrices using both loose (92%) and strict (97%) intensity thresholds and calculated Pearson and Spearman correlation coefficients alongside Manders' overlap metrics. Our results show that coarse resolution inflates apparent co-localization, particularly for Zn, which appears broadly distributed at 100  $\mu$ m but is confined to outer tissues at 5  $\mu$ m. In contrast, Ca-based overlaps remained stable across scales, while Fe–Mn pairs showed intermediate resolution sensitivity. This study demonstrates that the whole plant root may be analysed using the POLYX beamline setup with a multiresolution range (from 5  $\mu$ m). We show a methodological framework for micronutrient localization in roots of relatively large (beyond seedling) plants and offer first insights into potential differences in element heterogeneity that may result from the spatial regulation of nutrient uptake and transport, giving a preliminary framework for future studies.

topics: micro X-ray fluorescence ( $\mu$ XRF), synchrotron, micronutrients co-localization, plant metal homeostasis

## 1. Introduction

Life is fundamentally based on organic compounds composed of carbon, hydrogen, oxygen, nitrogen, phosphorus, and sulphur. These elements are essential for all organisms, yet they are not sufficient on their own. In plants, effective growth depends on a suite of essential mineral nutrients, including metallic elements (such as calcium, potassium, magnesium, iron, zinc, manganese, copper, nickel, and molybdenum), the metalloid boron, and the non-metal chlorine. These nutrients are traditionally classified as *macronutrients*, required in relatively high concentrations (C, H, O, N, P,

S, Ca, K, Mg), and *micronutrients*, required in trace amounts (B, Cl, Fe, Zn, Mn, Cu, Mo, Ni) (Table I) [1–3]. The concentrations of these nutrients in plants are highly dynamic and depend on plant species/variety, developmental stage, tissue type, and environmental factors such as substrate composition, pH, redox conditions, and water availability. Deviations from physiological ranges often result in deficiency or toxicity symptoms.

The environment from which plants acquire these nutrients is complex and heterogeneous. In addition to essential nutrients, it contains other elements that may be beneficial (e.g., Na, Si, Co, Se) or toxic (e.g., Cd, Pb), depending on concentration. Even essential or beneficial nutrients can become

TABLE I

Content of micro- and macroelements and their main functions in plants [1–3].

Macroelements	Dry matter content [mg/g]	Functional roles
carbon	$(4-5) \times 10^5$	Organic building blocks
oxygen	$(3.5-4.5) \times 10^5$	
hydrogen	$(0.6-0.7) \times 10^5$	
nitrogen	1–5	Major constituents of: <ul style="list-style-type: none"> <li>• macromolecules (e.g., proteins, nucleic acids, coenzymes, membrane components, chlorophyll)</li> <li>• organic metabolites (e.g., amino acids, amines, phytohormones, secondary metabolites)</li> <li>• signalling ions/molecules (e.g., <math>\text{NO}_3^-</math>, <math>\text{NH}_4^+</math>, NO)</li> </ul>
potassium	1–6	Osmotic regulation and providing turgor for cell growth Regulation of stomatal opening and plant movement Cation–anion balance, electro-neutrality, biochemical pH status Stabilization of binding between biomolecules
calcium	0.2–2	Structural element Stabilization of membranes, cell walls, and cytoskeleton Signalling ( $\text{Ca}^{2+}$ )
magnesium	0.1–1	Central element in chlorophyll Electrostatic interactions and complex formation with enzymes and substrates, for example adenosine triphosphate (ATP) activation through Mg-ATP complexation, essential for energy-requiring transport processes
sulphur	0.1–0.5	Constituent of organic metabolites and cellular components (e.g., cysteine, methionine, glutathione, ferredoxin, and secondary metabolites like glucosinolates)
phosphorus	0.3–0.5	Structural element of nucleic acids and phospholipids Energy metabolism (ATP and NADPH) Signalling and enzyme activation via phosphorylation and dephosphorylation
Microelements	Dry matter content [ $\mu\text{g/g}$ ]	Functional roles
chlorine	200–400	Catalyst in oxygen-evolving complex (OEC) Osmoregulation, maintaining turgor pressure and water balance in cells, especially in guard cells that regulate stomatal opening and closing
iron	50–500	Tetrapyrrole cofactor biosynthesis Chlorophyll biosynthesis Nitrogen and sulphur assimilation
zinc	30–100	Global catalytic and structural role in 10% of proteome Reactive oxygen species (ROS) scavenging Protein synthesis
manganese	20–200	Catalyst in OEC Lignin biosynthesis
boron	5–100	Stabilizing cell walls by cross-linking rhamnogalacturonan-II monomers into dimers
copper	2–20	Photosynthesis ROS scavenging Lignin polymerization
molybdenum	1–5	Nitrogen metabolism Nitrogen fixation
nickel	0.01–10	Nitrogen metabolism Detoxification of ROS

harmful when present in excess [4]. Understanding how plants regulate the uptake, transport, and spatial distribution of nutrients is therefore central to plant physiology and agriculture [5].

Our work focuses on the micronutrients Zn, Cu, Fe, and Mn, which are essential cofactors in diverse physiological processes. Zn contributes to transcriptional regulation through zinc-finger proteins and activates numerous dehydrogenases and hydrolases; Cu is indispensable for redox enzymes such as plastocyanin and superoxide dismutase, linking it to photosynthetic and oxidative stress pathways; Fe is central to chlorophyll biosynthesis, respiration, and electron transport via cytochromes and Fe-S proteins; Mn is required for the oxygen-evolving complex of photosystem II and for enzymes involved in the tricarboxylic acid cycle [1, 2, 6, 7]. We also examine Ca, which, beyond its structural role in cell walls and membranes, functions as a ubiquitous second messenger in signalling pathways that mediate plant responses to micronutrient deficiency. Including Ca in our analysis therefore provides a physiological context for interpreting the distribution of Zn, Cu, Fe, and Mn [2, 8]. These micronutrients (besides Ca) usually occur at low concentrations, making their detection and spatial mapping analytically challenging [9, 10]. While molecular biology has revealed much about the regulation of metal homeostasis, a complete understanding requires direct visualization of nutrient distributions within tissues, particularly in roots, which are difficult to extract and analyse without disturbing their native architecture.

Several methods have been developed to visualize elemental distributions in plants, each with its own strengths and limitations. *Autoradiography* allows tracing of radioisotope uptake and redistribution, with the advantage of distinguishing applied isotopes from native pools [11, 12]. However, it is limited to single elements, requires handling of radioactive materials, and typically achieves only  $\sim 100 \mu\text{m}$  resolution [13]. *Histochemical and fluorometric staining* methods, such as Perls/DAB for Fe [14] or fluorescent probes like Zinpyr-1 for Zn [15], provide qualitative localization but suffer from low sensitivity, potential chemical artefacts, and interference from autofluorescence [4, 16, 17]. *Electron microscopy coupled with energy-dispersive X-ray spectroscopy* (SEM/TEM-EDS) can achieve sub-micron resolution [9], but requires demanding cryofixation protocols to avoid elemental redistribution [18, 19]. Finally, *micro X-ray fluorescence* ( $\mu\text{XRF}$ ) has emerged as a powerful, non-destructive technique for mapping multiple elements simultaneously in hydrated tissues, with resolutions down to several micrometres on benchtop systems and even finer at synchrotron facilities [10, 20].

Despite these advances, significant gaps remain. Most available methods either sacrifice resolution for throughput or vice versa, and few offer a robust quantitative framework for comparing the

co-localization of multiple elements across spatial scales. Recently, we undertook a project aimed at investigating the regulation of Zn distribution within and between plant organs [21]. A central challenge was the ability to localize Zn at both the organ and tissue levels without introducing artefacts. Given the known limitations of various Zn detection methods, we prioritized minimizing sample preparation artefacts — especially Zn displacement during fixation, dehydration, or dye infiltration. To meet these requirements, we selected the newly commissioned POLYX beamline [19] (proposal 239061), which offered high sensitivity and spatial resolution for hydrated samples. Our previous work [21] revealed that Zn tends to accumulate in specific root tissues under heterogeneous soil conditions, highlighting the plant’s adaptive strategies for nutrient allocation, including altered expression of Zn homeostasis genes. In that study, we uncovered mechanisms governing Zn distribution across tissues and organs in environments that mimic natural soil variability, where localized zones of Zn enrichment coexist with deficient regions. In the present study, we build on this foundation by focusing on methodological optimization in preparing and analysing plant root samples at the POLYX beamline and extending the approach to a broader multi-element context.

To this end, we applied  $\mu\text{XRF}$  mapping combined with quantitative co-localization analysis to investigate the distributions of Zn, Cu, Fe, Mn, and Ca in plant roots. By comparing maps with coarse ( $100 \mu\text{m}$ ) and fine ( $5 \mu\text{m}$ ) resolutions, generating overlap matrices subject to strict and loose thresholding criteria, and calculating both correlation-based and fraction-based co-localization metrics, we provide a detailed account of how resolution influences the interpretation of nutrient co-distribution. This study establishes a methodological framework for multi-scale, multi-element  $\mu\text{XRF}$  mapping of plant roots. While the approach is inherently multi-elemental, Zn receives particular attention due to our focus on its homeostasis and the extensive prior knowledge available, which provides a strong interpretive reference point.

## 2. Methods

We study plant nutrient homeostasis using transparent soil (TS) [2], a medium that resembles natural soil but is sterile and has a fully adjustable nutrient composition. TS also enables the creation of heterogeneous biotic and abiotic environments. A particularly useful feature for our analyses is the ease of root cleaning — roots can be removed from the medium by simply rinsing them in distilled (DI) water. We used a modified Knop’s nutrient solution, as described earlier [22], with the following composition: 3 mM  $\text{Ca}(\text{NO}_3)_2 \cdot 4\text{H}_2\text{O}$ , 1.5 mM  $\text{KNO}_3$ , 1 mM

$\text{KH}_2\text{PO}_4$ , and 1.25 mM  $\text{MgSO}_4$ . The micronutrient stock contained 25  $\mu\text{M}$   $\text{H}_3\text{BO}_3$ , 2  $\mu\text{M}$   $\text{MnCl}_2 \cdot 4\text{H}_2\text{O}$ , 0.1  $\mu\text{M}$   $\text{CuSO}_4 \cdot 5\text{H}_2\text{O}$ , 0.5  $\mu\text{M}$   $\text{Na}_2\text{MoO}_4 \cdot 2\text{H}_2\text{O}$ , 5  $\mu\text{M}$  KI, and 0.1  $\mu\text{M}$   $\text{CoCl}_2 \cdot 6\text{H}_2\text{O}$ . In addition, 40  $\mu\text{M}$  Fe-EDTA and 4  $\mu\text{M}$   $\text{ZnSO}_4$  were supplied (1  $\mu\text{M}$   $\text{ZnSO}_4$  in the 14-strength Knop medium). The pH was adjusted to 5.8.

### 2.1. Preparation of transparent soil

Transparent soil was prepared by dropwise addition of a sodium alginate:Phytigel<sup>®</sup> (Sigma-Aldrich) mixture (1:4) into a 10 mM  $\text{MgCl}_2$  solution, which immediately polymerized the outer layer to form spherical beads, as described previously [23]. A sterile system described earlier [21] was used to produce large quantities of TS. Approximately 0.5 cm diameter TS beads were used. Beads were cross-linked for 4 h, rinsed with sterile DI water, and transferred to an equal volume of liquid half-strength Knop's medium with adjusted Zn concentration, i.e., 2  $\mu\text{M}$   $\text{ZnSO}_4$ . After diffusion, this yielded  $\frac{1}{4}$ -strength Knop's medium containing 1  $\mu\text{M}$   $\text{ZnSO}_4$ . Beads were left in the medium overnight to allow complete nutrient diffusion. For experimental setups, 200 g of beads were placed in Magenta<sup>®</sup> boxes. Residual fluid at the bottom was removed with a sterile pipette. Seedlings were positioned in holes made with a pipette tip.

### 2.2. Plant material and growth conditions

Experiments were conducted using tobacco (*Nicotiana tabacum* var. *Xanthi*). Plants were grown in a controlled-environment chamber under the following conditions: 23/16°C day/night temperature, 40–50% relative humidity, 16 h photoperiod, and photosynthetically active radiation (PAR) of 250  $\mu\text{mol}/(\text{m}^2 \text{ s})$  provided by fluorescent Flora tubes. Seeds were surface-sterilized in 8% (w/v, i.e., weight/volume) sodium hypochlorite for 2 min, rinsed, and germinated on vertically positioned Petri dishes containing  $\frac{1}{4}$ -strength Knop's medium supplemented with 2% (w/v) sucrose and 1% (w/v) agar. After three weeks, seedlings were transferred to TS in  $7 \times 10 \text{ cm}^2$  Magenta<sup>®</sup> boxes and grown for an additional two weeks (Fig. 1a).

### 2.3. Sample mounting

The experiment was conducted at the POLYX beamline to avoid artefacts from sample transfer, such as drying. Samples were rinsed in DI water to remove beads and mounted directly on the sample holder, fitted with a 3.6  $\mu\text{m}$   $\mu\text{XRF}$  foil (Spectro-Film<sup>™</sup>, DuPont) (Fig. 1b).

The 3D-printed square polymer holder ( $5 \times 5 \text{ cm}^2$  mounting space), materials used, and sample-mounting protocol are shown in Fig. 1b–e. To prevent drying during analysis, additional gel beads (without nutrients) were placed in the mounting setup. These beads did not interfere with measurements and extended the time before drying to up to 8 h. We used 5–6-week-old tobacco plant young roots that do not show secondary growth and have a diameter in the range of 200–400  $\mu\text{m}$ .

### 2.4. Beamline setup

Micro-XRF 2D mapping experiments were performed at the POLYX beamline of the SOLARIS National Synchrotron Radiation Centre [24, 25]. Monochromatic X-rays from the SOLARIS bending magnet (1.3 T) were generated using a Mo/ $\text{B}_4\text{C}$  multilayer monochromator (1.3% bandwidth). The beam was focused with ellipsoidal monocapillary optics (Sigray; 20 nm Pt inner coating; 20 mm working distance) to a focal spot of 5  $\mu\text{m}$ . For comparison, polycapillary optics (focal spot  $\sim 80 \mu\text{m}$  at 8 keV; IfG) were used as well, also providing 100  $\mu\text{m}$  resolution maps; however, 5  $\mu\text{m}$  resolution maps were not possible to achieve with polycapillary optics (see Fig. S1 in supplementary information [26]).

Samples were mounted on motorized translation stages for 2D scanning. For high-resolution maps with monocapillary optics, we used a 5  $\mu\text{m}$  scan step; for lower-resolution maps, we used 100  $\mu\text{m}$  scan step. Spectra were acquired with two Hitachi Vortex EM360 silicon drift detectors (ML3.3 Extreme; 25  $\mu\text{m}$  Be window; 0.5 mm Si sensor; 80<sup>2</sup> active area) coupled to an XGLab DANTE digital pulse processor. Detectors were positioned in backscattering geometry (45° to the sample surface), with the incident X-ray beam normal to the surface.

We performed tests of mono- and polycapillary optics using a root sample (see Fig. S1 in [26]). Zn, Fe, Ca, Mn, and Cu were chosen as ROI for fluorescence analysis. Polycapillary optics has larger transmission than monocapillary optics, but also a larger focal spot. Therefore, we observed a larger detection signal in XRF maps obtained with polycapillary optics. A diffused effect of these maps originates from the larger spot of polycapillary optics. Since monocapillary optics provides sufficient intensity but higher resolution, we chose the monocapillary setup for further analysis.

2D maps in this study were acquired in mapping mode with a fast continuous horizontal and vertical point-by-point motion. Low-resolution  $\mu\text{XRF}$  maps (for the whole root) were acquired using a resolution of 100  $\mu\text{m}$  (scan step) and an acquisition time of 12.5 ms per point (scan area around  $3.5 \times 3 \text{ cm}^2$ , total acquisition time 2–3 h).



Fig. 1. Experimental design for  $\mu$ XRF analysis of plant samples. (a) Schematic representation of the plant growth protocol leading up to  $\mu$ XRF analysis. (b) Material used for sample preparation, including the design of the custom sample holder with adjustable thickness; here, a 0.5 cm thickness was used. (c) Mounting procedure for basic support film onto the sample holder. (d) Configuration for mounting thick 3D samples, such as whole plants with leaves and roots. (e) Mounting approach for thin, flat samples, such as roots or organ cross-sections, using a dual-film “sandwich” technique.

High-resolution  $\mu$ XRF maps with detailed information were acquired with a 5  $\mu$ m scan step and 10 ms time per scan point (scan area around  $1.4 \times 1.3 \text{ mm}^2$ , total acquisition time 3–4 h). Count

rates in the selected energy regions of interest were normalized to detector live time and incident beam intensity (measured with an ionization chamber). Data from both detectors were summed, accounting

for differences in signal response due to different detector windows. Before experiments, detector energy calibration was performed using standard foils/samples for Zn, Fe, Cu, and Mn (Goodfellow).

It is important to note that at the incident energy used (12 keV), the synchrotron beam penetrates the full thickness of the young tobacco roots ( $\approx 200\text{--}400\ \mu\text{m}$ ). The effective sampling depth of the fluorescence signal is element-dependent, namely, low-energy lines such as Ca  $K_{\alpha}$  (3.7 keV) remain biased toward outer tissues, whereas higher-energy lines (Mn  $K_{\alpha}$  of 5.9 keV, Fe  $K_{\alpha}$  of 6.40 keV, Cu  $K_{\alpha}$  of 8.04 keV, Zn  $K_{\alpha}$  of 8.64 keV) approach whole-root cross-section integration [9, 27]. We included approximate fluorescence self-absorption calculations in hydrated plant tissue ( $\sim 90\%$  water,  $\rho \approx 1\ \text{g/cm}^3$ ) for Ca, Mn, Fe, Cu, and Zn  $K_{\alpha}$  lines at effective path lengths of 100, 200, and 400  $\mu\text{m}$ , and at  $45^\circ$  detection geometry in Table SI in supplementary information [26]. Thus, while all tissues are irradiated, the contribution of each tissue to the detected signal varies by element, and tissue-level assignments should be interpreted with this limitation in mind. Because the root shape is cylindrical (see Fig. S2 in supplementary information [26]), the detected fluorescence signal represents a superposition of contributions from multiple tissues along the electron escape path. Signals attributed to the epidermis can be interpreted with relatively high confidence, as they originate from the outermost layer; however, even here, some overlap from adjacent cortical tissue is unavoidable. Signals from the cortex represent an integration across several cortical cell layers and include contributions from the epidermis. Likewise, signals attributed to the vascular tissue overlap with the surrounding cortex and, indirectly, with epidermal contributions. If the vascular signal differs significantly from the cortical background, it can still be distinguished, but the interpretation must remain cautious. In addition, the higher cell density in the central region of the root (smaller, more numerous cells) increases the relative contribution of vascular signals in the middle of the cortex, providing some potential for interpretation, for example, by comparison with cortex/epidermis regions. For these reasons, tissue-level interpretation of elemental distributions should be considered semi-quantitative and element-dependent, with the clearest assignments at the epidermis and progressively greater overlap in deeper tissues.

## 2.5. Collecting data

Two initial measurements were performed to compare detector systems (polycapillary vs Sigray), as mentioned above. The same root sample was first analysed with the polycapillary setup and subsequently with the Sigray detector, which provided superior spatial resolution. Because the sample had

already been exposed for  $\sim 8\ \text{h}$  at that stage, no further biological interpretation was pursued. Instead, a new sample was introduced for the main analysis presented here. This study is therefore based on a *single dataset*, consistent with the methodological focus and the time limitations inherent to synchrotron beamtime. Broad-resolution studies take  $\approx 2\text{--}3\ \text{h}$  for the whole root, and detailed analysis takes another 3 h.

Importantly, the transparent soil comprises discrete hydrogel beads that create locally independent microenvironments. The analysed plant developed several lateral roots that colonized distinct bead domains, providing multiple, spatially separated segments of the root system within a single measurement. While this does not constitute formal biological replication, it offers internal technical consistency checks across lateral roots exposed to comparable medium composition at the growth box scale.

## 2.6. Data processing

At each scan position, an X-ray fluorescence spectrum was acquired. For each selected element, a region of interest (ROI) was defined around its characteristic fluorescence line, and the counts within this ROI were summed. The resulting count rates (scalar) were assigned to the corresponding pixel of the elemental XRF map for that element, so the pixel intensity was equal to the summed ROI counts. These maps were normalized and exported to `*.tiff` format using Matlab scripts at the beamline. Next, custom Python scripts were used to analyse the images. All codes used in the analysis are presented in Supplementary Information [26]. Briefly, for each resolution (i.e., 100  $\mu\text{m}$  and 5  $\mu\text{m}$ ), elemental distributions were exported as greyscale images, with pixel intensity proportional to the detected counts. To evaluate co-occurrence, overlap masks were generated by thresholding the elemental maps using two criteria, i.e., (i) a *loose threshold* (92%), which allowed for broader inclusion of signal and emphasized continuity, and (ii) a *strict threshold* (97%), which restricted overlaps to the most confident, high-intensity pixels. Pairwise overlap images were then assembled into matrices, with diagonal panels labelled by element, and off-diagonal panels showing the corresponding overlap masks. This approach provided a visual framework for comparing element-by-element co-localization across different resolutions.

Quantitative co-localization was assessed using three complementary measures:

- **Pearson correlation coefficient** — calculated for all pixels to capture the *linear relationship* between two elemental intensity distributions. High values indicate that strong signals in one element tend to coincide with strong signals in the other.

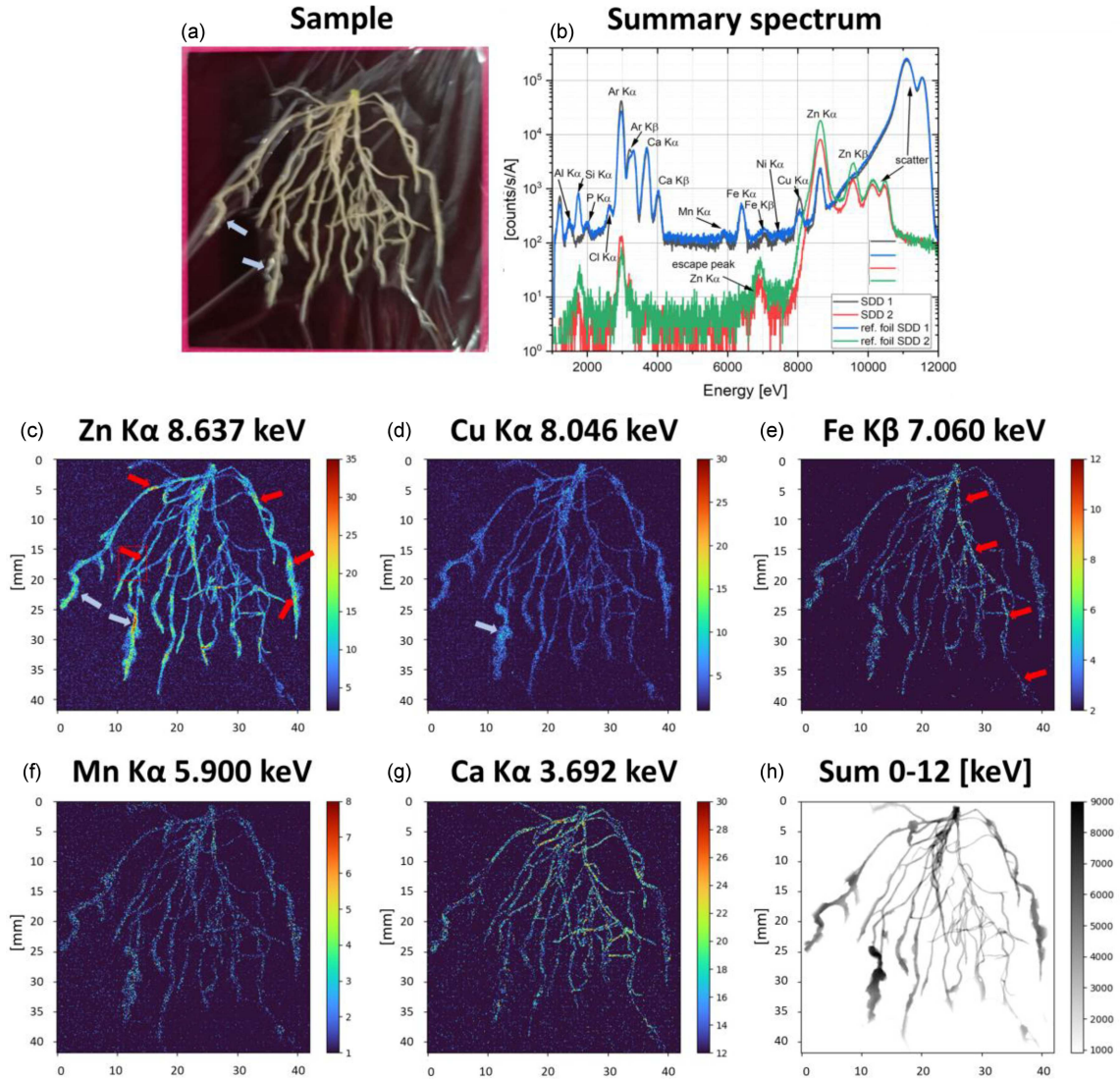


Fig. 2. Whole root  $\mu$ XFR mapping at coarse resolution ( $100\ \mu\text{m}$ ). (a) Image of the root system. (b) Summed XRF spectrum in the range 0–12 keV. (c–h) Distribution maps for elements: (c) zinc, (d) copper, (e) iron, (f) manganese, (g) calcium, and (h) their summed intensity. Brighter colours indicate a higher relative amount of the element. Coloured arrows and rectangle indicate regions described in the text.

- Spearman correlation coefficient — a *rank-based* measure that evaluates whether the ordering of pixel intensities is similar between two elements, regardless of the absolute values. This metric is less sensitive to non-linearities and outliers.
- Manders' coefficients ( $M_1$  and  $M_2$ ) — calculated at both loose and strict thresholds. Their values represent the *fraction of one element's signal that overlaps with another's signal*; thus,  $M_1$  quantifies the proportion of element A overlapping with element B, while  $M_2$  quantifies the inverse relationship.

To compare robustness across scales, we computed ratios of the metric values obtained at spatial resolution of  $100\ \mu\text{m}$  and  $5\ \mu\text{m}$ . This allowed us to distinguish element pairs whose apparent

co-localization was stable across resolutions from those whose overlap was inflated at coarse scale but diminished at fine scale.

### 3. Results

The results presented below derive from a single representative root sample analysed with the Sigray detector, selected after an initial detector comparison. These maps are intended to demonstrate the feasibility and optimization of the approach. Notably, several lateral roots extended into distinct bead domains of the transparent soil. Similar element distribution patterns were observed across these lateral roots, despite their spatial separation within the medium.

The following results are presented in a structured manner, beginning with whole-root maps, then zoomed-in regions, followed by overlap analyses and quantitative co-localization metrics. Within each section, observations are described element-by-element (or pair-by-pair in co-localization) to ensure clarity and consistency.

### 3.1. Low resolution (100 $\mu\text{m}$ ) — the “fast map” for the whole root system analysis

The plant root system was first analysed using low resolution (100  $\mu\text{m}$ ) to capture the whole sample (Fig. 2a). We first looked at the summed spectrum (Fig. 2b), demonstrating that our setup allows for reliable detection of several light elements (Al, Si, P, Cl, Ca) as well as heavier elements (Mn, Fe, Ni, Cu, Zn) at the monochromator energy of 12 keV. Potentially, by increasing the incident beam energy to 15 keV, it could be possible to extend the measurable range to include additional heavier elements, such as As and Se, and potentially also others, detectable at their L-edges (e.g., Mo, Cd, Pb), depending on experimental requirements.

The homeostasis of Zn, Fe, Mn, and Cu is closely interconnected and regulated by overlapping sets of membrane transporters [28]. This functional overlap underlies metal cross-homeostasis, where changes in the availability of one micronutrient can influence the uptake, distribution, and storage of others [28–34]. In this work, we chose Zn, Fe, Mn, and Cu to showcase the potential of  $\mu\text{XRF}$  mapping at the POLYX beamline for in planta simultaneous elemental distribution and co-localization analysis. These elements were selected due to their essential roles in plant physiology and their well-established interactions within metal homeostasis networks. We also added Ca, which is detected at high concentrations in the cell wall and can serve as a structural marker [35, 36]. Its distribution provides indirect information about cell wall thickness and the localization of de-methyl-esterified pectins, which bind  $\text{Ca}^{2+}$  to form cross-links that influence wall rigidity [36]. Since pectin structure and cell wall porosity can affect nutrient movement from the growth medium into root tissues, Ca mapping can also contribute to understanding the physical and chemical environment in which metal uptake occurs.

The low-resolution  $\mu\text{XRF}$  maps revealed the overall architecture of the root system by displaying the distribution of each analysed element (Fig. 2c–g). At this coarse resolution, the elemental maps highlight broad spatial patterns rather than fine structural details. Zn appeared widely distributed, following the main root axis and extending into lateral branches, suggesting an even Zn supply (Fig. 2c). Nevertheless, several Zn hotspots were observed (Fig. 2c, red/blue arrows). These hotspots may correspond to Zn uptake sites in direct contact with the

medium, as indicated in Fig. 2a and c (blue arrows), where remnants of gel beads are visible. Additional Zn hotspots potentially located in the basal root region may reflect Zn storage, consistent with previous reports of higher Zn accumulation in this part of the root [31]. Cu signals were overall weaker but still detectable in localized stretches, reflecting its lower abundance and more diffuse distribution (Fig. 2d). Interestingly, Cu intensity appeared higher in the medium (gel beads) than in the root itself (Fig. 2d, blue arrow indicating gel bead area).

Fe and Mn exhibited the least diffuse distributions (Fig. 2e–f). Notably, Fe showed the highest abundance among all analysed elements in the basal and middle regions of the main (longest) root (Fig. 2e, three red arrows indicating basal, middle, and apical parts). This pattern is consistent with the possibility of a root–shoot barrier for Fe transport or that the main root serves as the primary Fe storage site, although further replicated analyses would be required to confirm this. Mn showed the weakest signal without a clear specific localization. Ca traced the root structure more continuously than any other element, consistent with its structural role in cell walls and its abundance in plant tissues (Fig. 2g). Several Ca hotspots were also observed, although they were much smaller than the Zn hotspots (compare Fig. 2c and g). Finally, a map integrated over the entire energy spectrum range provided a structural reference, clearly outlining the entire root system and the residual gel beads (blue arrows), thereby enabling alignment of the elemental distributions with the visible root architecture or pointing at potential artefacts (Fig. 2h). Together, these maps show that all five elements are present throughout the root system. The 100  $\mu\text{m}$  maps provide a reliable overview of elemental presence and broad allocation of given element hot spots, which makes them perfect for choosing parts where tissue-level fine-scale analysis can be done.

### 3.2. Zooming in: finer detail at 5 $\mu\text{m}$

To resolve more localized patterns, a selected region of the root (Fig. 3a, red rectangle indicates ROI) was imaged at 5  $\mu\text{m}$  resolution. At this scale, Zn and Ca signals are strongest along the outer regions of the root, potentially indicating epidermal cells and localized Zn storage within some of them (Fig. 3b, f). As explained for the low-resolution image, the Zn-enriched sites may correspond to zones where the root was in direct contact with a bead surface. This hypothesis could be verified through in situ  $\mu\text{XRF}$  analysis; however, due to beamtime constraints, we plan to conduct such measurements in a future experiment. Interestingly, it seems that a relatively prominent Zn signal, which stretches along the root close to the lateral root emergence site, is localized in a region of the vascular tissue,

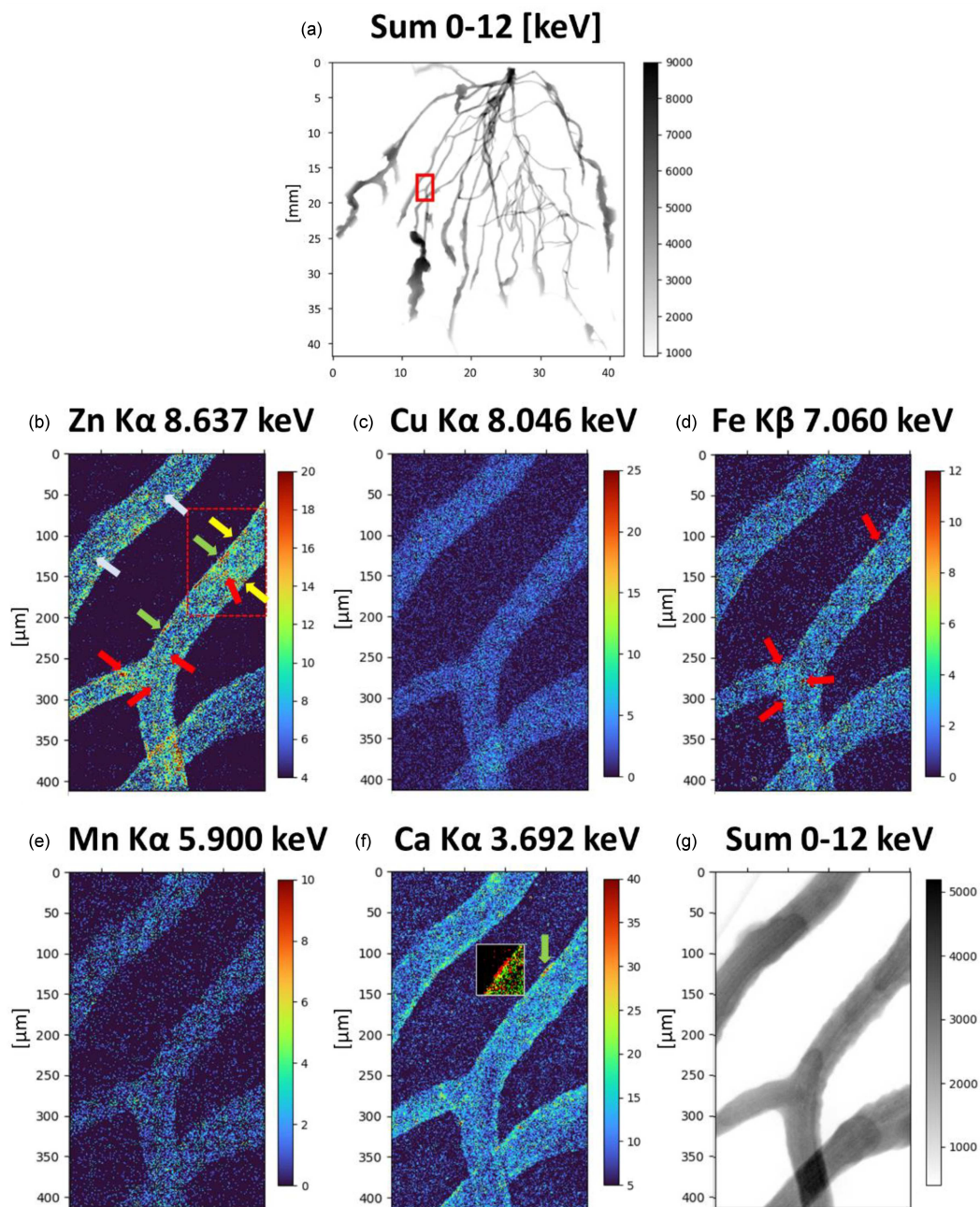


Fig. 3. Fine-scale  $\mu$ XRF mapping of a selected root region. (a) Summed intensity map of the region of interest (ROI) indicated by red rectangle. (b–f) Elemental distribution maps at  $5\ \mu\text{m}$  resolution for: (b) Zn, (c) Cu, (d) Fe, (e) Mn, and (f) Ca. (g) Summed intensity map of the zoomed region providing structural reference. Brighter colours indicate a higher relative amount of the element. Coloured arrows and rectangle indicate regions described in the text.

suggesting increased Zn level in those parts (Fig. 3b, red arrows). Moreover, in the root without a lateral root, this vascular Zn signal is missing (Fig. 3b, blue arrows). We also wanted to zoom in on the part of the root that shows an increased Zn signal (Zn hotspot) but does not have a gel bead leftover that could show an artificial signal (Fig. 2c, red rectangle; Fig. 3b, red rectangle). It is clear that the Zn hot spot signal is coming from the first several epidermal cells (Fig. 3b, yellow arrows) and potentially

spans across the cortex, up to the vascular tissue. However, this might be an effect of increased epidermal cell signal at the top (as roots are cylindrical, and the fluorescence signal comes from the whole shape). To further study this localization, we plan to analyse Zn at the root cross-section.

One of the highest Ca signals seems to be also localized in the same area as the high Zn epidermis cell signal (Fig. 3b, f, green arrows). Remarkably, at this resolution, it seems that the Zn signal (Fig. 3f,

green pixels in the square two-channel inset) comes from the cell, and the Ca signal (Fig. 3f, red pixels in the square two-channel inset) is localized in a linear structure around the cell, which would relate to the cell wall where the highest Ca levels are present [36].

Cu and Mn show a relatively uniform distribution (Fig. 3c, e). However, for Fe, several localized regions of high signal intensity are evident in relatively small spots (Fig. 3d, red arrows), along with one larger area of Fe accumulation.

This accumulation occurs in the same region of the root where the Zn hotspot was observed. Such localization is compatible with the interpretation that Fe and Mn may be continuously transported toward the vascular tissues and further to the shoot, rather than being stored in the epidermis and cortex; however, this remains to be tested in replicated experiments. Although the signal intensity and resolution for all elements shown in the analysis are not sufficient to indicate subcellular structures, finer detail suggests that the elements Zn, Fe, and Ca are not evenly distributed across the root, but instead exhibit preferential localization (Fig. 3b–f). The summary fluorescence map reveals some information about tissue elements with a central cylinder visible in the darker, middle region of the root (Fig. 3g). Compared with the low-resolution image of the same root, which shows continuous patterns at 100  $\mu\text{m}$ , the 5  $\mu\text{m}$  maps reveal a more fragmented and — particularly for Zn, Fe, and Ca — more heterogeneous distribution of these elements.

### 3.3. Where elements meet: overlap matrices at coarse scale

Simultaneous analysis of several elements at different scales enables the study of their co-localization at both the organ and tissue levels. Such information is crucial for disentangling element uptake sites, their storage locations, and patterns of abundance. To visualize how elements co-occur across the entire root system, overlap matrices were generated at 100  $\mu\text{m}$  resolution (Fig. 4 and also Fig. S3 for Ca in Supplementary Information [26]). Each off-diagonal panel represents the spatial intersection of two elemental maps, while the diagonal panels are labelled with the element names. At this coarse scale, the overlaps appear widespread and continuous, largely following the main and lateral roots. Under the “loose” criterion, the overlap regions are extensive, producing broad bands that suggest strong co-localization (Fig. 4a). Applying the “strict” criterion reduces the extent of these regions, but the overall impression remains that many elements appear to coincide across large parts of the root system (Fig. 4a).

Closer examination of individual element pairs shows that Ca tends to overlap with other elements in a similar pattern, reflecting calcium’s broad

distribution in cell walls and apoplastic spaces (see Fig. S3 in [26]). Only Ca–Zn co-localization appears to be enhanced, which likely reflects the fact that both elements exhibit the highest fluorescence signals. For Ca, this is due to its natural abundance and high concentration in the cell wall ( $\approx 1 \text{ mM}$  [37]).

For Zn, the effect arises because its fluorescence energy lies close to the monochromator excitation energy used during  $\mu\text{XRF}$  scanning, and is partially on the tail of the scatter peak, which increases emission efficiency and results in higher apparent intensity [38]. Consequently, Zn can dominate the signal in overlapping regions, making its distribution appear broader and more coincident with other elements than it truly is. This effect is particularly pronounced at coarse resolution with the “loose” criterion, where pixel averaging further amplifies the impression of co-localization. This effect was reduced using the “strict” criterion for co-localization. This adjustment balanced Ca co-localization with all elements, although it also lowered the overall degree of overlap. For all Zn pairs, the analysis revealed that high-Zn regions (Zn hotspots) may co-localize with other elements, but not within the main root (Fig. 4a, red arrows for lateral hot spots and blue for main root). This pattern is consistent with the possibility of shared transport pathways in lateral roots, although confirmation would require replicated analyses. These findings require further confirmation and additional studies. Fe–Mn overlaps are also present, but compared to Zn, they form continuous stretches along the roots. Cu–Fe and Cu–Mn overlaps show moderate overlap. Overall, the coarse-scale matrices emphasize continuity and significant overlap, but the smoothing effect of large pixels likely exaggerates the degree of true co-localization.

### 3.4. Sharper view: overlap matrices at fine scale

When the same analysis is applied to the zoomed region at 5  $\mu\text{m}$  resolution (Fig. 4b), a different picture emerges. Here, the overlap masks are thinner, more fragmented, and more localized. The strongest co-localization signal originates from overlapping roots, which we considered as an obvious artefact and excluded from the analysis. There is a clear artefact where, under the “loose” criterion, overlaps are still visible across much of the root cross-section, but they no longer form continuous bands. Instead, they appear as irregular patches or streaks, reflecting the finer spatial separation of elemental signals (Fig. 4b).

Under the “strict” criterion, the overlap regions shrink further, often appearing as small, isolated clusters rather than extended structures. This contrast with the 100  $\mu\text{m}$  matrices highlights how finer resolution reveals separation between elements that

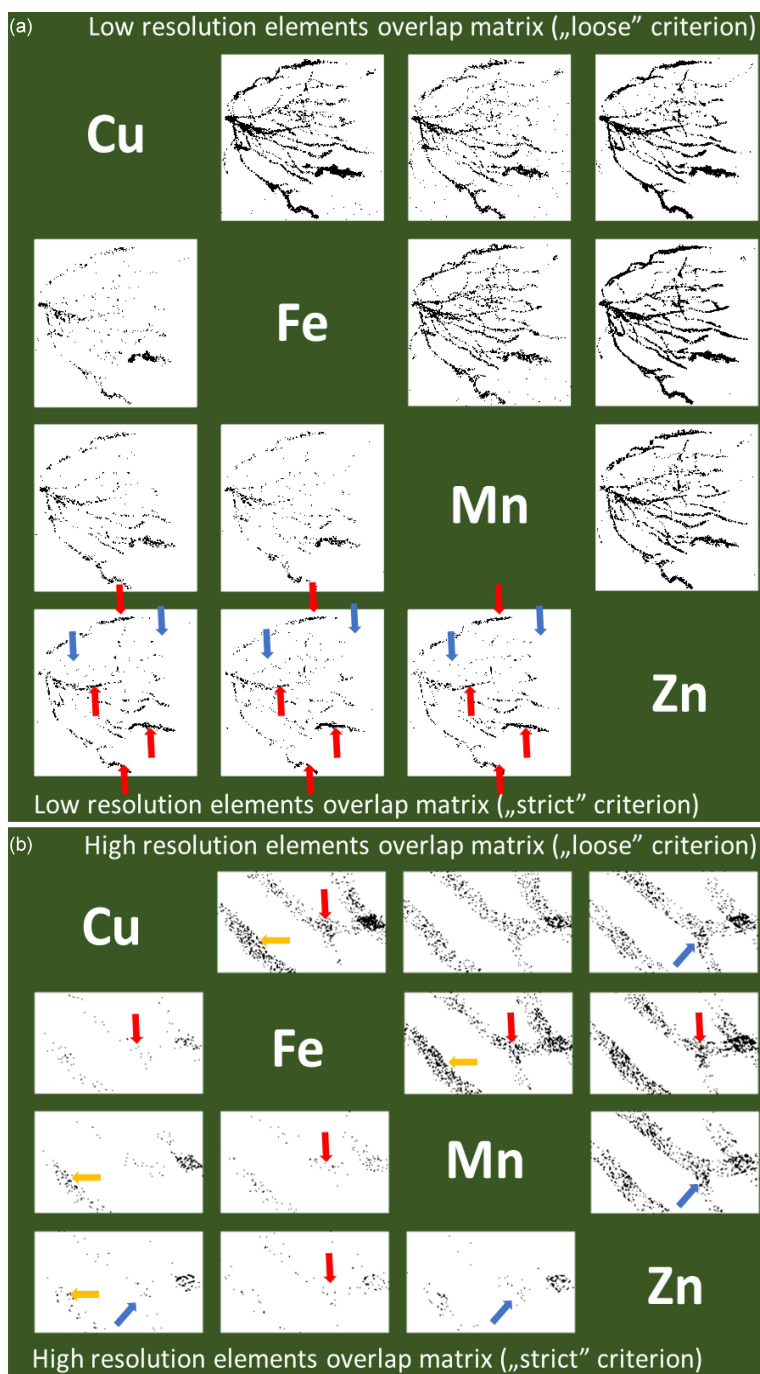


Fig. 4. Resolution-dependent co-localization matrices. Matrix overviews of overlap masks for all element pairs at resolutions (a) 100  $\mu\text{m}$  and (b) 5  $\mu\text{m}$ , shown respectively for strict (97%) and loose (92%) thresholds (as marked). Each off-diagonal cell displays the overlap mask for the corresponding element pair; diagonal cells are labelled with element names.

seemed to overlap at a coarser scale. Inspection of individual element pairs revealed that Ca still overlaps with each element (see Fig. S3 in [26]). However, Cu–Fe, Cu–Mn, and Fe–Zn also appear to overlap mostly in the central region where lateral roots emerge (Fig. 4b, red arrows). This localization is noteworthy and may indicate regions important for micronutrient delivery from lateral roots to higher-order roots. One possible explanation, which

will be tested in future work, is the involvement of Zrt-/Irt-like protein (ZIP) family transporters, which are known to mediate Zn, Fe, Mn, and Cu transport [34]. Interestingly, Cu–Fe and Fe–Mn show increased overlap in the lateral root that does not have an emerging lateral root (Fig. 4b, yellow arrows). Zn–Cu and Zn–Mn appear to co-localize in a distinct but nearby region compared to the previously described area, specifically in the basal part

of the newly emerging lateral root (Fig. 4b, blue arrows). This observation highlights a region that requires further investigation in future replicated studies. These fine-scale images emphasize the value of high-resolution  $\mu$ XRF studies in specific tissue regions that may play a critical role in micronutrient homeostasis.

### 3.5. From images to numbers: co-localization metrics

To move beyond visual impressions, co-localization was quantified using three complementary approaches: Pearson correlation, Spearman correlation, and Manders' coefficients (Fig. 5) [39]. Each metric captures a different aspect of how two elemental signals relate to one another. The *Pearson correlation coefficient* measures the linear relationship between pixel intensities in two channels, with values close to +1 indicating that high intensity in one element is consistently associated with high intensity in the other. The *Spearman correlation coefficient* is rank-based and less sensitive to absolute intensity — instead it reflects whether the ordering of pixel intensities is similar between two elements. This makes it more robust to non-linear relationships. The *Manders' coefficients* ( $M_1$  and  $M_2$ ) quantify the fraction of one element's signal that overlaps with another, under either a loose or strict threshold. Loose thresholds include more pixels and tend to yield higher values, while strict thresholds restrict the analysis to the brightest, most confident pixels, producing lower but more conservative estimates of overlap.

At the coarse scale 100  $\mu$ m, all three metrics tended to be higher, reflecting the inflated overlaps seen in the matrices (Fig. 5a, b, e, g). Large pixels merge signals from adjacent tissues, artificially increasing both correlation and overlap fractions. At 5  $\mu$ m, the values were consistently lower and more variable, consistent with the fragmented and localized overlap patterns observed in the finer maps (Fig. 5b, e, g). This confirms that resolution strongly affects the apparent degree of co-localization. Analysed element by element, Ca-based pairs (Ca–Cu, Ca–Fe, Ca–Mn) consistently showed the highest stability across scales and thresholds. Pearson and Spearman correlations remained moderate to high, and Manders' coefficients changed little between loose and strict criteria. This suggests that calcium's distribution is relatively uniform and overlaps broadly with other elements, regardless of the resolution. Fe and Mn also showed strong correlations at 100  $\mu$ m, with Pearson and Spearman values indicating a close relationship (Fig. 5a, e, g, h). However, at 5  $\mu$ m, both correlations and Manders' coefficients dropped, especially under strict thresholds, revealing that their

apparent overlap at coarse scale was partly due to pixel averaging (Fig. 5b, e, g). Cu–Fe and Cu–Mn pairs retained moderate correlations across scales, but Cu–Zn pairs were highly resolution-dependent. At 100  $\mu$ m, Pearson and Manders values suggested strong overlap, but at 5  $\mu$ m, both metrics fell sharply, particularly under strict thresholds, showing that the apparent co-localization was largely an artefact of pixel size (Fig. 5e–h). Zn was the most sensitive element overall. Pairs involving Zn (especially Fe–Zn and Mn–Zn) had high Manders' coefficients under loose thresholds at 100  $\mu$ m, but these values collapsed under strict thresholds at 5  $\mu$ m. Pearson and Spearman correlations followed the same trend, dropping from moderate at coarse scale to weak at fine scale (Fig. 5e–h). This indicates that zinc's distribution is more confined to specific regions, and its overlap with other elements is easily overestimated at low resolution.

Together, these analyses show that Ca emerges as the most stable co-localization “partner”, while Zn is the most variable, with overlaps that appear strong at 100  $\mu$ m but largely disappear at 5  $\mu$ m. This underscores the importance of integrating multiple spatial scales, highlighting the utility of the POLYX beamline  $\mu$ XRF capabilities for investigating micronutrient dynamics.

### 3.6. Ranking robustness: other ways to show the stability of element pairs

Finally, stability scores were calculated by combining the ratios of metrics between both 100  $\mu$ m and 5  $\mu$ m resolutions (Fig. 5i–l). The bar chart ranks element pairs by their combined stability. Calcium-based pairs, particularly Ca–Fe, Ca–Cu, and Ca–Mn, emerge as the most stable, showing relatively consistent overlap across scales. In contrast, pairs involving zinc, especially Fe–Zn and Mn–Zn, are the least stable, with overlaps that appear strong at 100  $\mu$ m but diminish markedly at 5  $\mu$ m. This ranking formalizes the visual impression from the matrices and provides a clear framework for comparing how different elements co-localize in the root system.

## 4. Discussion

The elemental maps and co-localization analyses presented here provide a multi-scale view of nutrient distribution in plant roots. By combining whole-root imaging at 100  $\mu$ m with high-resolution mapping at 5  $\mu$ m, it is possible to compare broad architectural patterns with more localized elemental distributions. The  $\mu$ XRF provides a unique capability to perform such measurements relatively quickly and without extensive sample preparation [27].

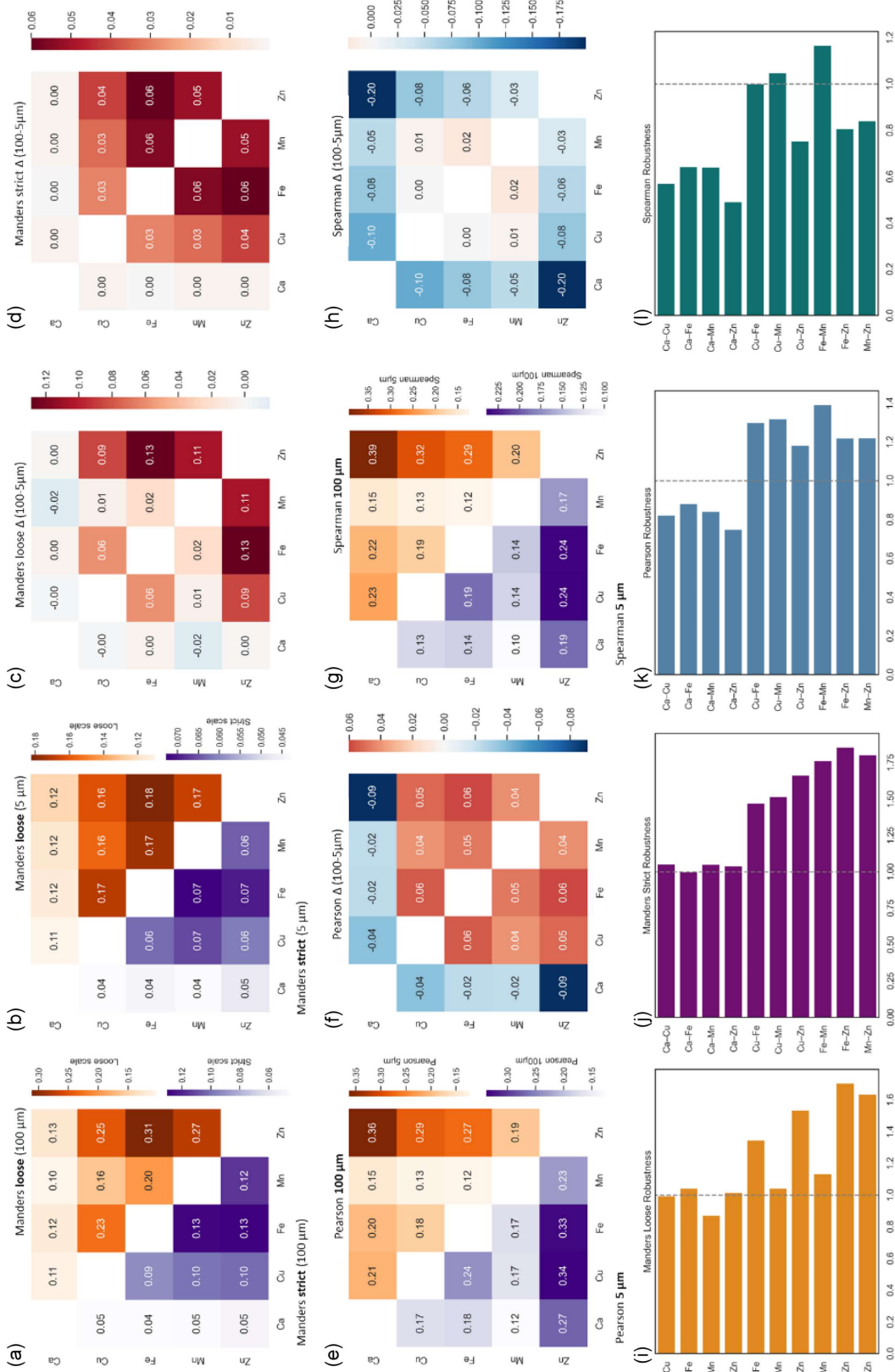


Fig. 5. Resolution-dependent co-localization of Ca, Cu, Fe, Mn, and Zn at 5 μm and 10 μm. Heatmaps summarize: Manders coefficients with loose/strict threshold at (a) 100 μm and (b) 5 μm; (c) Manders loose threshold difference, Δ(100-5) μm; (d) Manders strict threshold difference, Δ(100-5) μm; (e) Pearson correlation (5 μm/100 μm); (f) Pearson correlation resolution difference, Δ(100-5) μm; (g) Spearman correlation (5 μm/100 μm); (h) Spearman correlation resolution difference, Δ(100-5) μm. Robustness bar charts for (i) Manders with loose threshold, (j) Manders with strict threshold, and for (k) Pearson and (l) Spearman coefficients.

The POLYX beamline, which allows for hydrated sample measurements at both scales in a relatively short time, seems to be a perfect setup for analysing plant nutrient homeostasis. For comparison, in a reasonable time (up to 12 h), a bench-top system provides an analysis area of only around  $1 \times 1 \text{ cm}^2$  [10]. On the other hand, large synchrotrons offer fast scan time; however, sample size is even more limiting (for more details about synchrotron-based techniques, see [27]). POLYX seems to find a middle ground between analysis time and sample size.

From a root biology perspective, our multi-scale  $\mu\text{XRF}$  analysis revealed distinct spatial patterns of micronutrient distribution within the root system, reflecting anatomical constraints. At a coarse resolution of  $100 \mu\text{m}$ , Zn was the most widely distributed trace element. It was, however, mostly pronounced in lateral roots, with hotspots that may correspond to uptake sites in direct contact with the growth medium, consistent with earlier reports of localized Zn transporter expression in those regions [31, 40]. It should be noted that a strong signal is, at large, a result of the closeness of the Zn  $K_\alpha$  fluorescence peak (8.637 keV) to the peak originating from the scattered incident X-ray beam (12 keV), and thus, being on its tail, the intensity of the Zn signal may rise with the total intensity of the scattered radiation [38].

Cu signals were weaker and more diffuse, with higher intensity in the surrounding medium than in the root itself, in line with its low abundance and strict homeostatic regulation [41, 42]. Fe showed the highest presence in the main root, and there was usually more Fe in the basal part of the lateral roots. This pattern is consistent with the possibility of preferential Fe storage in the main root and localized control over Fe translocation near the basal regions of lateral roots, although further replicated analyses are needed to confirm this. It was reported that the functioning of Fe transports, such as iron-regulated transporter 1 (IRT1), in roots of *Arabidopsis thaliana* is controlled systemically by Fe sufficiency/deficiency signals [43]. Fe is also stored to support plant development in the vacuole, and this is supported by vacuolar iron transporter AtVIT1, which is expressed strongly in roots and vasculature of shoots [44]. This indicates that there are ready mechanisms to detect Fe sufficiency/deficiency and control its storage and distribution. Our preliminary results could lead our molecular studies of Fe homeostasis in the direction of the basal part of the main and lateral roots, where Fe seems to be stored in larger quantities. Mn signals were weakest and lacked clear localization, reflecting their potential mobility and low concentration requirements [7, 8]. Ca traced the root structure most continuously, highlighting its structural role in cell walls, with small hotspots consistent with localized enrichment [9, 10].

High-resolution ( $5 \mu\text{m}$ ) imaging provided finer detail, revealing that Zn and Ca were strongly localized in outer root regions, likely epidermal cells, with Zn hotspots extending toward vascular tissues near lateral root emergence sites. This suggests that Zn uptake and radial transfer are spatially linked to vascular loading [11]. Moreover, Ca signals that seem to co-localize with Zn at the epidermis were in fact not directly overlapping, with Zn being inside the cell and Ca in the apoplast. This observation may indicate that epidermal cells with elevated Zn uptake also possess thicker cell walls, as suggested by increased Ca signal, but this remains a hypothesis requiring targeted validation. Cell wall consists of cellulose, hemicellulose, and pectin that create a gel-like matrix cross-linked by divalent ions [35, 45]. Zn has a higher affinity for binding to pectin than Ca, and therefore cell wall pectin may serve as a Zn retention site. For example, it was recently shown that adjustment of pectin methylesterification, which modulates the capacity for Zn binding, represents a mechanism of plant tolerance to elevated Zn levels [46]. Since plants are sessile organisms, this may indicate plant preparedness for the situation when Zn uptake sites become Zn toxicity sites that plants need to cope with. Fe hotspots were observed in regions corresponding to Zn, indicating possible shared distribution pathways or localized storage in cells close to vascular tissues [47, 48]. By contrast, Cu and Mn remained relatively uniform, supporting the view that their concentrations and potential for storage are limited but also less spatially restricted [49, 50].

Elemental overlap analysis further emphasized the importance of imaging resolution. At  $100 \mu\text{m}$ , overlaps appeared broad and continuous, particularly for Ca paired with other elements, but this was partly an artefact of pixel averaging and Zn fluorescence efficiency (these were shown and reviewed before [13, 27, 51]). At  $5 \mu\text{m}$ , overlaps were more fragmented and localized, with notable co-localization of Fe–Zn, Cu–Fe, and Cu–Mn in regions near lateral root emergence. These sites may represent candidate junctions for micronutrient transfer from lateral roots into the main vascular pathway. Further studies should first focus on synchrotron-based determination of element distributions in hydrated samples, followed by the identification of element co-localization and the isolation of specific tissues for quantitative polymerase chain reaction (PCR) analysis of ZIP, HMA, and YSL family transporters (HMA — Heavy Metal ATPase, YSL — Yellow Stripe-Like), which are known to mediate the transport of multiple divalent cations [21, 28, 36, 52]. Such an approach would provide much-needed insights into the potential distribution mechanisms of these ions.

Together, these findings highlight the methodological value of combining coarse and fine  $\mu\text{XRF}$  mapping. The  $100 \mu\text{m}$  “fast maps” provide a reliable overview of elemental allocation across the root

system, while the 5  $\mu\text{m}$  maps uncover tissue-level heterogeneity and potential functional hotspots. Although based on a single representative analysis, the concordance across lateral roots and the consistency of multi-scale patterns support the robustness of the approach. This work, therefore, provides a methodological framework and proof-of-concept for future replicated studies aimed at linking elemental imaging with molecular mechanisms of nutrient homeostasis.

Our results showed that at the coarse scale, the elemental distributions largely followed the visible root system. Zn, Ca, Fe, Mn, and Cu all appeared to trace the main and lateral root, giving the impression of widespread overlap. This is not surprising, as 100  $\mu\text{m}$  pixels integrate signals across multiple tissues, effectively merging adjacent zones into a single one. The overlap matrices at this scale reinforced this impression; under both “loose” and “strict” criteria, large regions of the root appeared to contain coincident signals from multiple elements. Such images are useful for capturing the overall nutrient status of the root system.

The finer 5  $\mu\text{m}$  maps revealed a more complex picture. At this resolution, elemental distributions were no longer continuous along the root axis but instead appeared fragmented and heterogeneous. Taken together, these results demonstrate the value of combining multi-scale imaging with quantitative co-localization analysis. Whole-root maps provide a useful overview, but finer resolution is essential for revealing tissue-level differences and avoiding overestimation of overlap. The stability ranking offers a framework for identifying which element pairs are robust across scales and which are highly resolution-dependent. This approach could be extended to other plant species, growth conditions, or nutrient treatments, providing a general strategy for linking elemental imaging with functional interpretation.

Finally, the study underscores the importance of methodological transparency in co-localization analysis. Threshold choice, pixel size, and the definition of overlap all influence the outcome. By explicitly comparing strict and loose criteria, and by quantifying stability across resolutions, we provide a more nuanced picture of elemental co-distribution in roots. This framework not only strengthens the interpretation of the present data but also offers a template for future studies aiming to connect elemental imaging with plant physiology.

## 5. Conclusions

The results presented here are based on a single representative analysis and should be regarded as a methodological proof-of-concept for the analysis of the whole root system using  $\mu\text{XRF}$ . Using the POLYX beamline at NSRC SOLARIS, which allows for combining whole-root and high-resolution

elemental mapping with quantitative co-localization analysis, this study showed a multi-scale view of nutrient distribution in plant roots. At coarse resolution (100  $\mu\text{m}$ ), elemental maps and overlap matrices suggested widespread co-occurrence of Zn, Cu, Fe, Mn, and Ca across the root system. However, higher-resolution imaging (5  $\mu\text{m}$ ) revealed that these apparent overlaps often break down into more localized and heterogeneous patterns, with elements showing preferential enrichment in different regions of the root. Together, these findings highlight the importance of simultaneous analysis across multiple scales for the interpretation of elemental imaging data. Whole-root maps provide valuable overviews, but higher resolution is essential for uncovering tissue-level differences in nutrient distribution and for revealing previously unknown mechanisms. The initial results presented here serve as a proof-of-concept and an introduction to broader studies on plant metal cross-homeostasis. The POLYX beamline appears to be an ideal tool for pursuing this line of investigation in greater depth.

## Acknowledgments

The authors thank Nina Adamek-Siwirykow, Martyna Siwik, and Małgorzata Palusińska for their help, especially during beamtime.

This research was supported by the National Science Centre, Poland, under project nos. 2020/39/D/NZ9/02393 and 2023/51/B/NZ9/02518.

Research at the National Synchrotron Radiation Centre SOLARIS is supported by the Ministry of Science and Higher Education, Poland, under contract no. 1/SOL/2021/2.

## References

- [1] G.H. Lilay, N. Thiébaud, D. du Mee, A.G.L. Assunção, J.K. Schjoerring, S. Husted, D.P. Persson, *New Phytol.* **242**, 881 (2024).
- [2] T.C. De Bang, S. Husted, K.H. Laursen, D.P. Persson, J.K. Schjoerring, *New Phytol.* **229**, 2446 (2021).
- [3] A.V. Barker, D.J. Pilbeam, *Handbook of Plant Nutrition*, CRC press, 2007.
- [4] O. Siemianowski, A. Barabasz, A. Weremczuk, A. Ruszczyńska, E. Bulska, L.E. Williams, D.M. Antosiewicz, *Plant Cell Environ.* **36**, 1093 (2013).
- [5] M.G. Palmgren, S. Clemens, L.E. Williams, U. Krämer, S. Borg, J.K. Schjoerring, D. Sanders *Trends Plant Sci.* **13**, 464 (2008).

- [6] H. Kaur, H. Kaur, H. Kaur, S. Srivastava, *Plant Growth Regul.* **100**, 219 (2023).
- [7] E. Andresen, E. Peiter, H. Küpper, *J. Exp. Bot.* **69**, 909 (2018).
- [8] K. Thor, *Front. Plant Sci.* **10**, 440 (2019).
- [9] A. van Der Ent, W.J. Przybyłowicz, M.D. de Jonge, H.H. Harris, C.G. Ryan, G. Tylko, D.J. Paterson, A.D. Barnabas, P.M. Kopittke, J. Mesjasz-Przybyłowicz, *New Phytol.* **218**, 432 (2018).
- [10] A. Mijovilovich, F. Morina, S.N. Bokhari, T. Wolff, H. Küpper, *Plant Methods* **16**, 82 (2020).
- [11] T.L. Read, C.L. Doolette, N.R. Howell, P.M. Kopittke, T. Cresswell, E. Lombi, *Environ. Sci. Technol.* **55**, 13523 (2021).
- [12] E.G. Solon, A. Schweitzer, M. Stoeckli, B. Prideaux, *AAPS J.* **12**, 11 (2010).
- [13] E. Lombi, K.G. Scheckel, I.M. Kempson, *Environ. Exp. Bot.* **72**, 3 (2011).
- [14] H. Roschttardt, G. Conéjéro, C. Curie, S. Mari, *Plant Physiol.* **151**, 1329 (2009).
- [15] S.A. Sinclair, S.M. Sherson, R. Jarvis, J. Camakaris, C.S. Cobbett, *New Phytol.* **174**, e22681 (2007).
- [16] H. Roschttardt, G. Conéjéro, F. Divol, C. Alcon, J.-L. Verdeil, C. Curie, S. Mari, *Front. Plant Sci.* **4**, 350 (2013).
- [17] O. Siemianowski, A. Barabasz, M. Kendziorek, A. Ruszczyńska, E. Bulska, L.E. Williams, D.M. Antosiewicz, *J. Exp. Bot.* **65**, 1125 (2014).
- [18] S. Mishra, G. Wellenreuther, J. Mattusch, H.-J. Stärk, H. Küpper, *Plant Physiol.* **163**, 1396 (2013).
- [19] I. Hurbain, M. Sachse, *Biol. Cell* **103**, 405 (2011).
- [20] F. Morina, A. Kuvelja, D. Brückner, M. Mojović, Đ. Nakarada, S.N.H. Bokhari, B. Vujić, G. Falkenberg, H. Küpper, *New Phytol.* **246**, 2222 (2025).
- [21] M. Pypka, D. Davydenko, K. Sowa, J. Maksymiuk, P. Wróbel, T. Kołodziej, P. Korecki, O. Siemianowski, *BMC Plant Biol.* **25**, 1341 (2025).
- [22] A. Barabasz, U. Krämer, M. Hanikenne, J. Rudzka, D.M. Antosiewicz, *J. Exp. Bot.* **61**, 3057 (2010).
- [23] L. Ma, Y. Shi, O. Siemianowski, B. Yuan, T.K. Egner, S.V. Mirnezami, K.R. Lind, B. Ganapathysubramanian, V. Venditti, L. Cademartiri, *Proc. Natl. Acad. Sci.* **116**, 11063 (2019).
- [24] K. Sowa, P. Wróbel, T. Kołodziej, W. Błachucki, F. Kosiorowski, M. Zając, P. Korecki, *Nucl. Instrum. Methods Phys. Res. B* **538**, 131 (2023).
- [25] J. Szlachetko, J. Szade, E. Beyer et al., *Eur. Phys. J. Plus* **138**, 10 (2023).
- [26] M. Pypka, A. Barabasz, K. Sowa, P. Wróbel, T. Kołodziej, P. Korecki, O. Siemianowski, *Acta Phys. Pol. A* **149**, S218.S1 (2026).
- [27] P.M. Kopittke, T. Punshon, D.J. Paterson, R.V. Tappero, P. Wang, F.P.C. Blamey, A. van der Ent, E. Lombi, *Plant Physiol.* **178**, 507 (2018).
- [28] D.M. Antosiewicz, A. Barabasz, O. Siemianowski, *Front. Plant Sci.* **5**, 80 (2014).
- [29] A. Papierniak, K. Kozak, M. Kendziorek, A. Barabasz M. Palusińska, J. Tiuryn, B. Paterczyk, L.E. Williams, D.M. Antosiewicz, *Front. Plant Sci.* **9**, 185 (2018).
- [30] A. Barabasz, M. Palusińska, A. Papierniak, M. Kendziorek, K. Kozak, L.E. Williams, D.M. Antosiewicz, *Front. Plant Sci.* **9**, 1984 (2019).
- [31] M. Palusińska, A. Barabasz, K. Kozak, A. Papierniak, K. Maślińska, D.M. Antosiewicz, *BMC Plant Biol.* **20**, 37 (2020).
- [32] K. Maślińska-Gromadka, A. Barabasz, M. Palusińska, K. Kozak, D.M. Antosiewicz, *Int. J. Mol. Sci.* **22**, 5355 (2021).
- [33] K. Kozak, A. Papierniak-Wyglądala, M. Palusińska, A. Barabasz, D.M. Antosiewicz, *Front. Plant Sci.* **13**, 867967 (2022).
- [34] M. Palusińska, A. Barabasz, D.M. Antosiewicz, *Metallomics* **16**, mfae035 (2024).
- [35] S. Rongpipi, W.J. Barnes, O. Siemianowski et al., *Front. Plant Sci.* **14**, 1212126 (2023).
- [36] O. Siemianowski, S. Rongpipi, J.T. Del Mundo G. Freychet, M. Zhernenkov, E.D. Gomez, E.W. Gomez, C.T. Anderson *JACS Au* **4**, 177 (2024).
- [37] C.T. Anderson, *J. Exp. Bot.* **67**, 495 (2016).
- [38] M.F. González, N. Saadatkhah, G.S. Patience, *Can. J. Chem. Eng.* **102**, 2004 (2024).
- [39] K.W. Dunn, M.M. Kamocka, J.H. McDonald, *Am. J. Physiol. Cell Physiol.* **300**, C723 (2011).
- [40] S.A. Sinclair, U. Krämer, *Biochim. Biophys. Acta Mol. Cell Res.* **1823**, 1553 (2012).
- [41] M. Pilon, *New Phytol.* **192**, 305 (2011).
- [42] K. Ravet, M. Pilon, *Antioxid. Redox Signal.* **19**, 919 (2013).
- [43] R. Tabata, T. Kamiya, S. Imoto et al., *Plant Cell Physiol.* **63**, 842 (2022).
- [44] S.A. Kim, T. Punshon, A. Lanzirrotti, L. Li, J.M. Alonso, J.R. Ecker, J. Kaplan, M.L. Guerinot, *Science* **314**, 1295 (2006).

- [45] S. Rongpipi, W.J. Barnes, O. Siemianowski et al., *Cellulose* **31**, 1397 (2024).
- [46] K. Zhong, P. Zhang, X. Wei et al., *Nat. Commun.* **15**, 5823 (2024).
- [47] U. Krämer, *Annu. Rev. Plant Biol.* **75**, 27 (2024).
- [48] M. Hanikenne, F. Bouché, *J. Exp. Bot.* **74**, 5426 (2023).
- [49] S. Puig, L. Peñarrubia, *Curr. Opin. Plant Biol.* **12**, 299 (2009).
- [50] J.K. Pittman, *New Phytol.* **167**, 733 (2005).
- [51] E. Lombi, J. Susini, *Plant, Soil* **320**, 1 (2009).
- [52] O. Siemianowski, R.F. Mills, L.E. Williams, D.M. Antosiewicz, *Plant Biotechnol. J.* **9**, 64 (2011).